**III**

Publication III

S. von Alfthan, F. Boxberg, K. Kaski, A. Kuronen, R. Tereshonkov, J. Tulkki and H. Sakaki, *Electronic, optical, and structural properties of quantum wire superlattices on vicinal (111) GaAs substrates*, Physical Review **B 72**, 045329 (2005).

# Electronic, optical, and structural properties of quantum wire superlattices on vicinal (111) GaAs substrates

S. v Alfthan, F. Boxberg,* K. Kaski, A. Kuronen, R. Tereshonkov,† and J. Tulkki
*Laboratory of Computational Engineering, Helsinki University of Technology, FIN-02015 HUT, Finland*

H. Sakaki
*Institute of Industrial Science, University of Tokyo, 4-6-1 Komaba, Meguro-ku, Tokyo, 153-8505, Japan*

We have studied corrugated quantum wells as a semiconductor quantum wire structure. The quantum well corrugation results from a step bunching effect during epitaxial growth on vicinal (111) GaAs substrates and might be used to form a quantum wire superlattice. The strain and piezoelectric effects were studied both by an atomistic valence force field method and by an elastic continuum model. Within the elastic continuum model we also studied the electromechanical coupling. The electronic band structure was calculated with the eight-band $\mathbf{k}\cdot\mathbf{p}$ model. The nonphysical oscillating solutions were eliminated by appropriate fine tuning of the material parameters. We have also studied the density of states and the polarization dependence of interband light absorption in the electric dipole approximation.

## I. INTRODUCTION

Fabrication techniques of semiconductor quantum wires (QWR) are presently subject of intensive research since their electronic and optical properties[1] can be achieved only if the material boundaries of the QWR structure are atomistically accurate and if the crystal structure is defect-free. Fabrication of high-quality nanometer-scale structures is very difficult using conventional processing techniques based on lithography and etching. Self-organized growth of low-dimensional structures has therefore been studied widely as an alternative approach.[2–5] The benefits of self-organized epitaxy, based on either molecular beam epitaxy (MBE) or metallorganic vapor phase epitaxy (MOVPE), are an almost defect-free crystal and a single-stage fabrication process.

In this paper we have studied a self-assembled quantum wire superlattice (QWRS) which forms as a result of atomic step bunching during epitaxial growth on a vicinal (111) GaAs substrate. Previously, the step bunching effect has been used to fabricate corrugated heterojunctions, creating both corrugated two-dimensional electron gases (2DEG) (Ref. 6) and one-dimensional QWRs.[7] GaAs and AlGaAs have been grown successfully on vicinal (111) substrates using MBE. During this process the add-on atoms were self-organized, creating a corrugated surface, consisting mainly of (111) and (110) crystal planes. Here we focus on quantum well (QW) structures defined by two corrugated material interfaces. Corrugated interfaces might give rise to QWRSs in which the wires would be aligned, with the direction depending purely on the substrate orientation.

The goal of the present work is to optimize the geometry and material composition to achieve as strong QWR confinement as possible. In our calculations we account for the band edge discontinuity, strain-induced band modification. Our calculations are based on fully three-dimensional strain analysis and we also include a comparison between atomistic and continuum elasticity models. The piezoelectric effect, which in the 8-band $\mathbf{k}\cdot\mathbf{p}$ analysis gives a large effect on the electronic structure,[8] has been fully taken into account in our calculations. For previous works on eight-band $\mathbf{k}\cdot\mathbf{p}$ calculations for QWR see, e.g., Refs. 9 and 10, and references therein.

## II. THE GEOMETRY OF THE QWRS

Figure 1(a) shows schematically the geometry of the most general idealized QWRS. The upper and the lower QW-barrier interfaces are identical, consisting of (111) and (110) planes. The QW, i.e., the shaded volume in Fig. 1(b), is taken to be $In_xGa_{1-x}As$. The barrier material of our calculations is $Al_xGa_{1-x}As$, shown with gray color in Figs. 1(b)–1(d). The geometry of Fig. 1(a) will be called corrugated-corrugated structure (CC structure).

For comparison we consider also the QWRS with a single planar QW-barrier interface, called corrugated-planar structure (CP structure). This QWRS was taken for closer numerical study, because it presumably could be fabricated easier of III–V materials. We considered the CP structure for two different material configurations: Fig. 1(c) called CP1 and Fig. 1(d) called CP2.

In our calculations we have varied the period of corrugation $P_{QW}$, the thickness of the quantum well $T_{QW}$, the phase shift between the two interfaces, and the material. The period and step height of the corrugation are directly related to the offset angle $\theta$ of the substrate.

## III. STRAIN CALCULATIONS

The strain in the QWRS structure was calculated using an atomistic energy minimization with a valence force field potential (VFF) and using a finite element (FE) method under the elastic continuum (EC) approximation. We used both methods for the structures in Fig. 1 in order to check the accuracy of our results for very thin QW structures.
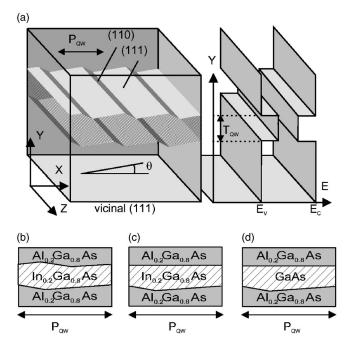
FIG. 1. The QWRS geometry. (a) 3D CC structure, (b) CC structure (strained), (c) CP1 structure (strained), (d) CP2 structure (lattice matched). The shaded region between the corrugated surfaces is the quantum well, $P_{QW} = 13.2$ nm is the period of the corrugation, $T_{QW} = 8$ nm is the thickness of the quantum well, and $\theta$ is the offset angle of the vicinal (111) substrate. The corrugated material interfaces are formed from (111) and (110) lattice planes.

The advantages of the EC method are the good availability of experimental parameters and the possibility to include piezoelectric coupling, but the disadvantage is that it excludes atomic scale information. We used the macroscopic Hooke's law extended with the piezoelectric coupling

$$\begin{pmatrix} (T) \\ (D) \end{pmatrix} = \begin{bmatrix} [C] & [e] \\ [e]^T & -[\varepsilon] \end{bmatrix} \begin{pmatrix} (S) \\ -(E) \end{pmatrix}. \tag{1}$$

In Eq. (1), $(T)$ is the stress vector, $(D)$ is the electric flux vector, $(S)$ is the strain vector, and $(E)$ is the electric field vector. Furthermore, $[C]$ is the elasticity matrix, $[e]$ is the piezoelectric matrix, and $[\varepsilon]$ is the dielectric matrix. This equation was solved iteratively with the commercial software Ansys,[11] using tetrahedral second order elements such that the total element mesh included about 1500 elements for one period of the geometry. The lattice mismatch was introduced by expanding the $In_xGa_{1-x}As$ isotropically by

$$\Delta a = \frac{a_{[In_xGa_{1-x}As]} - a_{[Al_yGa_{1-y}As]}}{a_{[In_xGa_{1-x}As]}} \tag{2}$$

and keeping the $Al_yGa_{1-x}As$ unchanged. In Eq. (2), $a_{[i]}$ is the lattice constant of material $i$.

For the interatomic potential we used the Keating VFF potential.[12,13] It expresses the energy of the crystal as a function of the nearest neighbors, containing a two-body part describing the effect of bond stretching and a three-body part describing bond bending

$$V_{pot} = \frac{1}{2} \sum_i^N \sum_j^{nn} \frac{3\alpha_{ij}}{8(d_{ij}^0)^2} [(r_{ij})^2 - (d_{ij}^0)^2]^2$$
$$+ \sum_i^N \sum_j^{nn} \sum_{k>j}^{nn} \frac{3\beta_{ij}}{8d_{ij}^0 d_{ik}^0} \left[ r_{ij}r_{ik} \cos\theta - \frac{1}{3}d_{ij}^0 d_{ik}^0 \right]^2, \tag{3}$$

where $r_{ij}$ is the calculated true distance and $d_{ij}^0$ the equilibrium distance between atoms $i$ and $j$. The factor $1/3$ in the bond bending term is the cosine of the ideal bond angle. The parameters $\alpha$ and $\beta$ of Eq. (3) were calculated by fitting the potential to the macroscopic elastic constants of the material. Moreover, we approximated alloys of type $A_xB_{1-x}C$ by an effective binary alloy with only $AB$ and $C$ atoms which are thought to form an ideal zinc blende structure. Potential parameters for this effective material were fitted to the elastic constants of Vegard's law[14] for the $A_xB_{1-x}C$ alloy.

The equilibrium structure of this model was obtained by minimizing the total potential energy using the conjugate gradient method (CG).[15] The local strain, at each atom, was calculated from the relative difference between the deformed atomic bonds and those of a strain-free crystal.

The atomistic calculations contained one rectangular period of the structure and were performed using periodic boundary conditions in $x$ direction and open boundary conditions in $y$ direction (orthogonal to the substrate surface).

## IV. ELECTRONIC STRUCTURE CALCULATIONS

The electronic structure of the QWRS was calculated using the eight-band $\mathbf{k} \cdot \mathbf{p}$ method.[16–18] In the confinement potential we accounted for the band edge discontinuity, strain induced deformation potential and piezoelectric potential. The total eight-band $\mathbf{k} \cdot \mathbf{p}$ Hamiltonian consists of a nonstrain and a strain part. The nonstrain part is parameterized by the band gap $E_g$, the spin-orbit (SO) splitting energy $\Delta$, the optical matrix element $E_p$, the VB potential $E_v$, the three modified Luttinger parameters $\gamma_1$, $\gamma_2$, and $\gamma_3$, the related conduction band (CB) parameter $\gamma_c$ and the Kane parameter B. The strain part is parameterized by the hydrostatic CB deformation potential $a_c$, the hydrostatic band gap deformation potential $a_g$, the valence band (VB) deformation potentials $b_v$ and $d_v$. The six components of the strain tensor $\varepsilon_{xx}$, $\varepsilon_{yy}$, $\varepsilon_{zz}$, $\varepsilon_{xy}$, $\varepsilon_{yz}$, $\varepsilon_{xz}$, and the piezoelectric potential $\phi_{piez}$ were obtained from the strain analysis and included in the strain Hamiltonian.

Expansion of the bulk CB energy as a quadratic function of the wave vector components $k_i$, $i = x, y, z$ gives the following connection between $\gamma_c$, the Kane parameter $A'$ and the CB effective mass $m_e$:

$$\gamma_c = \frac{2m_0}{\hbar^2} A' = \frac{1}{m_e} - \frac{E_p}{E_g} \frac{E_g + 2\Delta/3}{E_g + \Delta}. \tag{4}$$

The modified Luttinger parameters are related to the Luttinger parameters $\gamma_i^L$ as

$$\gamma_1 = \gamma_1^L - \frac{E_p}{3E_g}, \tag{5}$$

$$\gamma_2 = \gamma_2^L - \frac{E_p}{6E_g}, \tag{6}$$

$$\gamma_3 = \gamma_3^L - \frac{E_p}{6E_g}. \tag{7}$$

We set the parameter B equal to zero since its effect on the energy bands in zinc blendelike crystals has been reported to be negligible.[17]

Each matrix element of the total eight-band **k·p** Hamiltonian for bulk is a function of 19 parameters and the three components $k_x$, $k_y$, and $k_z$ of the wave vector. The transition from the bulk **k·p** Hamiltonian to the QWR **k·p** Hamiltonian is made by replacing the wave vector components $k_x$ and $k_y$ by the derivatives $-i(\partial/\partial x)$ and $-i(\partial/\partial y)$, correspondingly. In this procedure the matrix elements become differential operators and since the parameters vary spatially, we symmetrize each term containing derivatives, to retain the hermiticity of the Hamiltonian, as proposed by Stier and Burt.[17,19]

There are several ways to discretize the symmetrized Hamiltonian. In the finite differences (FD) calculations we replaced the diagonal second order derivatives ($\partial/\partial r_i Q \partial/\partial r_i$, $i=x,y,z$, $Q$—is a material parameter) by combinations of the standard first order forward $\partial_i^{(+)}$ and backward $\partial_i^{(-)}$ difference quotients as given by Stier[17]

$$\partial_{r_i} Q \partial_{r_i} \rightarrow [\partial_{r_i}^{(+)} Q \partial_{r_i}^{(-)} + \partial_{r_i}^{(-)} Q \partial_{r_i}^{(+)}]/2. \tag{8}$$

In counter distinction to Stier we replaced the first order derivatives and the second order mixed derivatives by the standard first order centered difference quotient $\partial_i^{(c)}$:

$$\partial_{r_i} Q + Q \partial_{r_i} \rightarrow \partial_{r_i}^{(c)} Q + Q \partial_{r_i}^{(c)} \tag{9}$$

and

$$\partial_{r_i} Q \partial_{r_j} \rightarrow \partial_{r_i}^{(c)} Q \partial_{r_j}^{(c)}. \tag{10}$$

Stier[17] used a different discretization schema for the upper right triangular and the lower down triangular matrices of the Hamiltonian

$$D_{r_i}^{(u)} = [\partial_{r_i}^{(+)} Q + Q \partial_{r_i}^{(+)}]/2, \tag{11}$$

$$D_{r_i}^{(l)} = [\partial_{r_i}^{(-)} Q + Q \partial_{r_i}^{(-)}]/2, \tag{12}$$

and

$$\partial_{r_i} Q \partial_{r_j} = [\partial_{r_i}^{(+)} Q \partial_{r_j}^{(+)} + \partial_{r_j}^{(+)} Q \partial_{r_i}^{(+)} + \partial_{r_i}^{(-)} Q \partial_{r_j}^{(-)} + \partial_{r_j}^{(-)} Q \partial_{r_i}^{(-)}]/4, \tag{13}$$

where $i=x,y,z$, and $D_{r_i}^{(m)}$, $m=l,u$ stands for a discretization of the lower down triangular and the upper right triangular matrices of the Hamiltonian, respectively.

We made test calculations for selected quantum structures of even symmetry and found that discretization based on Eqs. (11) and (12) leads to electron densities which do not have the symmetry of the quantum structure. This can be understood by considering a discretized QW **k·p** Hamiltonian in the x direction. The eight-band **k·p** Hamiltonian possesses inversion symmetry while the matrix of the FD discretized Hamiltonian lacks it. We observed furthermore that the use of Stier's discretization schema is less sensitive to the spurious oscillations which are due to the the eight-band **k·p** method. This feature will be discussed in more details in Sec. VI.

We accounted for the crystal orientation by applying a coordinate transformation rotating the eight-band Hamiltonan to the main axes of the crystal lattice.[20] Periodic boundary conditions were used in the x direction and Dirichlet boundary conditions (the eigenstates vanish at the boundary) in the y direction. The numerical matrix diagonalization was done using the implicitly restarted Lanczos method[21] implemented on a Beowulf Alpha parallel computer.

## V. CALCULATION OF DENSITY OF STATES AND ABSORPTION COEFFICIENT

The density of states (DOS) per area of the QWRS was calculated by summing over the pertinent subbands and integrating over **k**.[22] The DOS in the conduction bands is given by

$$g_C(E) = \sum_n \int_{E_{Cn}(k_x,k_z)<E_{C,B}} \frac{dk_x dk_z}{(2\pi)^2} \delta[E_{Cn}(k_x,k_z) - E], \tag{14}$$

where $E_{C,B}$ is the conduction band edge of the barrier material and the sum over n contains also the summation over spin. A similar expression is obtained for the DOS of the valence bands

$$g_V(E) = \sum_n \int_{E_{Vn}(k_x,k_z)>E_{V,B}} \frac{dk_x dk_z}{(2\pi)^2} \delta[E_{Vn}(k_x,k_z) - E], \tag{15}$$

where $E_{V,B}$ is the valence band edge of the barrier material.

The polarization of light absorption was calculated by integrating the optical transition dipoles over **k** for all interband transitions. The total absorption, as a function of energy E, is given by

$$A(E) = \frac{e^2\hbar}{2\pi^2 m_0^2 T_{QW} P_{QW} E} \sqrt{\frac{\mu}{\varepsilon}}$$
$$\times \sum_{n,m} \int dk_x dk_z |\mathbf{W}_{Cn,Vm}(k_x,k_z)|^2, \tag{16}$$

where $E_{Cn,Vm}$ is the transition energy, $\mu$ is the permeability, $\epsilon$ is the dielectric constant, and $W_{Cn,Vm}$ is the optical transition dipole between the nth conduction and the mth valence band. We have intentionally omitted any linewidth broadening in order to reveal the fine structure of the absorption. A more detailed description of the calculations of DOS and optical properties in the **k·p** model will be published elsewhere.[23]

## VI. MATERIAL PARAMETERS AND THEIR RELATION TO SPURIOUS OSCILLATIONS

All material parameters used in the **k·p** model are given in Table I. The parameters of the ternary compounds have

TABLE I. Material parameters used. The data is taken from Ref. 30 unless otherwise noted.

| Parameter | $Al_{0.2}Ga_{0.8}As$ | GaAs | $In_{0.2}Ga_{0.8}As$ |
|---|---|---|---|
| $E_g$ (eV) | 1.800 | 1.519 | 1.221 |
| $\Delta$ (eV) | 0.316 | 0.340 | 0.326 |
| $\gamma_1^L$ | 5.996 | 7.1 | 8.165 |
| $\gamma_2^L$ | 1.631 | 2.02 | 2.380 |
| $\gamma_3^L$ | 2.432 | 2.91 | 3.369 |
| $m_e$ | 0.082 | 0.063 | 0.055 |
| $E_p$ (eV) | 24.3 | 20.7 | 20.7 |
| VBO (eV)[a] | −0.906 | −0.8 | −0.758 |
| $a_v$ (eV) | 1.16 | 0.3 | 0.38 |
| $a_c$ (eV) | −7.17 | −6.66 | −7.188 |
| $b_v$ (eV) | −1.7 | −1.2 | −1.36 |
| $d_v$ (eV) | −4.6 | −3.6 | −1.98 |
| $c_{11}$ ($10^{11}$ dyn cm$^{-2}$) | 12.02 | 11.9 | 11.186 |
| $c_{12}$ ($10^{11}$ dyn cm$^{-2}$) | 5.372 | 5.38 | 5.209 |
| $c_{44}$ ($10^{11}$ dyn cm$^{-2}$) | 5.844 | 5.95 | 5.552 |
| $e_{14}$ (C m$^{-2}$) | −0.173[b] | −0.16 | −0.137 |
| $\varepsilon_r$ | 12.036 | 12.53 | 12.924 |

[a]Reference 31.
[b]Interpolated between AlAs from Ref. 32 and GaAs from Ref. 30.

been obtained by interpolation of the corresponding parameters for binary compounds (GaAs, InAs, and AlAs). The parameters in Table I are based on both experimental and theoretical works. Their quality has been tested for the dispersion of electronic bands in bulk semiconductors near the $\Gamma$ point.

In our test calculations, based on the material parameters given in Table I, we found for the structures of CC, CP1, and CP2 the high frequency ($f \cong 1/\Delta x$, where $\Delta x$ is the FD discretization step) spurious oscillating eigenfunctions corresponding to eigenvalues (in most cases) inside the band gap. Any rapidly oscillating solution of the envelope Hamiltonian suggests a correspondence with a high $k$-value solution of the bulk Hamiltonian. Similar nonphysical eigenstates have been reported by several groups for different semiconductor quantum structures and their origin has recently been subject of intense discussion. There have been several approaches to explain them: influence of boundary conditions,[24–26] limitations of the finite difference method,[27] a too high order of polynomial dependence of the bulk dispersion on the $k$ vector.[28] Furthermore, several methods were proposed to eliminate the spurious oscillations: to reduce the bulk band dispersion to a lower polynomial,[28] expand the envelope functions in plane waves and solve the new eigenvalue problem,[24] or simply to reject the spurious states.[29]

In order to study the origin of the nonphysical solutions, we used a separate two band model Hamiltonian for a QW (similar to the one used by Foreman).[28] We solved the eigenstates of this model Hamiltonian for different values of material parameters by using both the FD and FE methods. A comparison of our FD and FE method calculations showed that spurious oscillating eigenstates appear in the same way
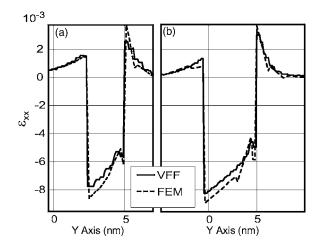


FIG. 2. The strain component $\varepsilon_{xx}$ in the crystal coordinate system along the vertical line shown in Fig. 3. In (a) the thickness is $T_{QW}=3$ nm, and in (b) $T_{QW}=6$ nm. The VFF and FEM results are shown by solid and dashed lines, respectively.

in both methods. Both methods become more sensitive to oscillating solutions when the number of grid points or the number of elements is increased. This is understandable since the accurate numerical description of rapidly oscillating functions is not possible with few grid points or elements. We conclude that these "spurious states" are actually real eigenstates of a "faulty" Hamiltonian and the oscillations observed in our calculations cannot be explained by the discretization approach. To find the origin of the nonphysical states we varied the values of material parameters and compared the results of our two-band model for the QW and the corresponding bulk material. We found that the spurious states tended to appear (for the same values of material parameters) in the QW calculations when for nonzero $k$ values (1) we obtain bulk band energies within the band gap or (2) the bulk electron energy has a local minimum (conduction band) or maximum (valence band).

On the basis of these numerical experiments it is obvious that the origin of the nonphysical solutions is in the use of
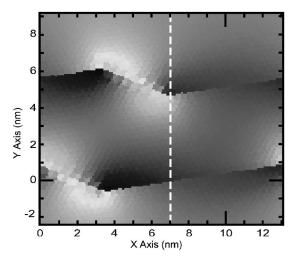


FIG. 3. The strain component $\varepsilon_{xx}$ calculated with VFF method for $T_{QW}=6$ nm. The results of Fig. 2 were plotted along the dashed line shown here.
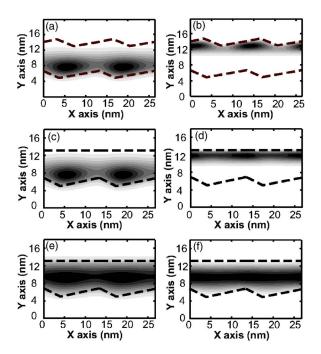
FIG. 4. The probability density of the electron ground states for the (a) strain CC, (c) strained CP1, (e) lattice-matched CP2 structure and (b), (d), and (f) show the corresponding probability density of the hole ground states, for **k**=0. The contour scale is linear (arbitrary units) and the black colour represents the maximum amplitude of each plot. The black dashed lines show the geometry used in the calculation.

eight-band **k·p** Hamiltonian which is only valid close to the Γ point. The low dimension of the QWRS leads to quantized states with an effective wave length corresponding to $k$ values beyond the limit of applicability of the eight-band **k·p** method. A consistent generic solution of this problem would be to start from a full band **k·p** model and to use it as the starting point of the envelope wave function method. In our work we obtained a working eight-band **k·p** Hamiltonian by adjusting the material parameters in such a way that the bulk electron dispersion did not have either of the symptoms (1) or (2). As a further condition we required that the near Γ-point bulk dispersion of the conduction and valence band fits the effective masses of Landolt–Börnstein.[30]

The spurious oscillations were eliminated by adjusting Kane's matrix element $E_p$ and recalculating $\gamma_c$ and the modified Luttinger parameters according to Eqs. (4)–(7). Other parameters were kept unchanged. We found that decreasing $E_p$ by 20% from the value given in Table I did not affect the eigenenergies very much (about 1 meV for ground states) but eliminated the spurious ones.

## VII. RESULTS AND DISCUSSION

In Fig. 2 we compare the strain component $\varepsilon_{xx}$, calculated by the VFF and FE methods for a CC structure with $T_{QW}$=3 nm [Fig. 2(a)] and $T_{QW}$=6 nm [Fig. 2(b)]. The strain component $\varepsilon_{xx}$ is plotted along a vertical line perpendicular to the QW plane through an apex in the QW-barrier interface (shown by a dashed line in Fig. 3). As can be seen from Fig.
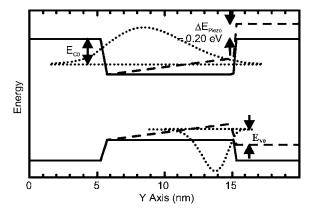


FIG. 5. Schematic picture of the band edge for the strained CC structure. The solid lines represent the band edges excluding strain effects. The dashed line shows the effect of the piezoelectric field. The piezoelectric potential energy difference across the well is $\Delta E_{piezo}$=0.20 eV. The probability density of the ground states of the conduction and valence bands are shown by dotted lines and the definition of the confinement energies $E_{C0}$ and $E_{V0}$ are shown by arrows.

2, the largest difference between the strain models is due to the limitations of the potential of the VFF model, giving rise to slightly different elastic constants in the two models. It is also obvious that, except for the material boundaries, the
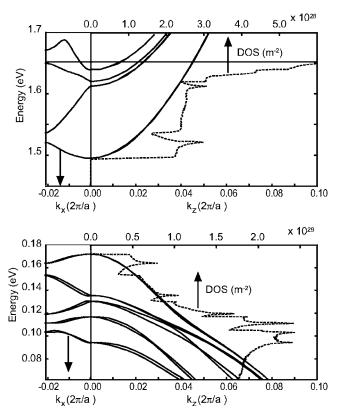


FIG. 6. The band diagram (solid lines) and DOS (dotted lines) for the strained CC structure. The band energy is given with respect to the strain-free valence band edge of bulk $Al_{0.2}Ga_{0.8}As$. The axis below the panels correspond to the wave vector of the energy bands and the axis at the top correspond to the DOS. The energy scale to the left is common to all curves.
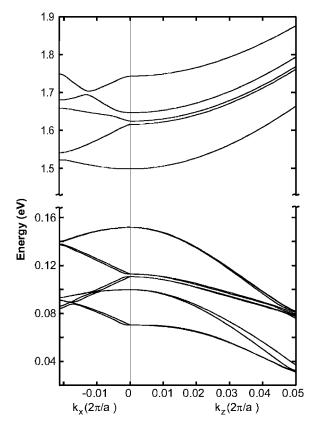
FIG. 7. The band diagram for the strained CP1 structure. The band energy is given with respect to the unstrained valence band edge of bulk $Al_{0.2}Ga_{0.8}As$.



FIG. 8. The band diagram for the strained CP2 structure. The band energy is given with respect to the valence band edge of bulk $Al_{0.2}Ga_{0.8}As$.

difference between the two models are due to the incomplete fitting of bulk elastic constants in the VFF model. The difference in the middle of the QW is almost the same for both QW thicknesses. EC calculations often give higher values right at the interfaces since the strain is not well defined here for the atomistic model. In the other strain components and in QW's of different sizes the same trend was repeated. Figure 3 shows the strain component $\varepsilon_{xx}$ in the complete structure. We conclude that, EC and atomistic calculations are in fair agreement for all studied geometries.[33]

In the EC calculations we accounted for the electromechanical coupling of the piezoelectric field and the off-diagonal strain components. The coupling itself is due to the ionic character of the bonds of the III–V compound semiconductors. The effect of the coupling on the strain components is, however, small. For the material compositions and geometries studied in this work the relative change in the strain, caused by the electromechanical coupling is typically less than 1%. Close to the sharp apexes of the QWRS, where the off-diagonal strain components and the field are big, the effect of the coupling is likely to exceed 1%. However, these geometrical singularity points can only be modeled exactly within an atomistic strain model accounting for the piezoelectric coupling. This is a topic for future work.

The probability densities of the lowest confined states are depicted in Figs. 4(a)–4(f). Figure 5 shows schematically the band edge and the definition of the confinement energy for the geometry of Figs. 1(b) and 1(c). The piezoelectric field in
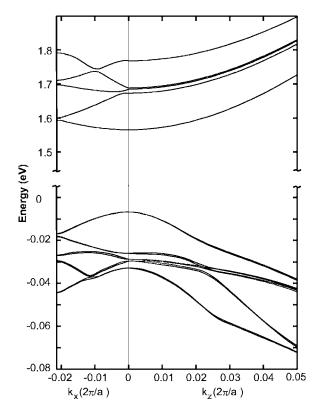
the active area was on the average 20 meV/nm resulting in a potential energy difference of 0.2 eV across the QW. This electric field strongly affects the carrier densities in the QW, spatially separating electrons and holes. Figures 6–9 show the energy dispersion of the lowest electron and hole states for two periods of the structures Figs. 1(b), 1(c), and 1(d).
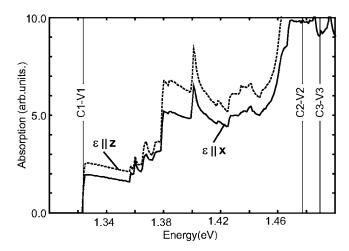


FIG. 9. Absorption coefficient for the strained CC structure of Fig. 1(b). The solid and dotted lines correspond to the absorption of light polarized in $x$ and $z$ directions, respectively ($z$ is parallel to the QWRS). The absorption coefficient was calculated without any linewidth broadening in order not to smear out the fine structure. The vertical lines indicate the energies of the diagonal transitions at $\mathbf{k}=0$.

TABLE II. The conduction and valence band ground state energies, QW confinement energies (CE), and effective masses.

| Geometry | Band | Carrier density | Energy (eV) | CE (eV) | $m_x^*$ $(m_0)$ | $m_z^*$ $(m_0)$ |
|---|---|---|---|---|---|---|
| Fig. 1(b) | CB Fig. 6 | Fig. 4(a) | 1.496 | 0.164 | 0.072 | 0.066 |
| | VB Fig. 6 | Fig. 4(b) | 0.172 | 0.122 | −0.293 | −0.113 |
| Fig. 1(c) | CB Fig. 7 | Fig. 4(c) | 1.498 | 0.162 | 0.073 | 0.067 |
| | VB Fig. 7 | Fig. 4(d) | 0.152 | 0.126 | −0.197 | −0.114 |
| Fig. 1(d) | CB Fig. 8 | Fig. 4(e) | 1.565 | 0.129 | 0.067 | 0.066 |
| | VB Fig. 8 | Fig. 4(f) | −0.069 | 0.037 | −0.155 | −0.118 |

The conduction and valence band ground state energies, QW confinement energies and relative effective masses $m_x^*$ and $m_z^*$ are given in Table II.

As shown in Figs. 6–8 the bands twice degenerate a $\mathbf{k}=0$ are splitted for high $k$ values. This feature has been discussed both within Rashba Hamiltonian[34] (single band case) and multiband $\mathbf{k}\cdot\mathbf{p}$ models.[27,35] We found in the present study that the origin of this splitting is in the asymmetry of the QWRS. The splitting is increased with increasing the asymmetry of the structure. Note that the expectation value of the spin is determined by $\langle s_z \rangle = \Sigma_{j=1}^8 \int |\Phi_j(x,y)|^2 dx dy \times \langle u_{j0}|s_z|u_{j0}\rangle$, where $\Phi_j$ are the enve-
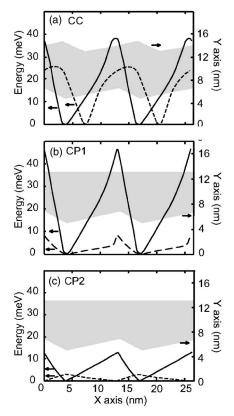


FIG. 10. Effective potential energy of an electron (solid line) and a hole (dashed line) as a function of $x$ coordinate, in (a) the strained CC, (b) the strained CP1, and (c) the lattice-matched CP2 structure. The shaded areas and the $y$ axis to the right show the corresponding geometry.

lope functions, and $u_{j0}$ are the Bloch functions at $\Gamma$ point. Therefore, both of the splitted states include some contribution of both spin components.

The dashed lines and the top axes of Fig. 6 correspond to the electron and hole DOS of the corresponding QWRS. The DOS shows signatures of both one-dimensional (1D) and two-dimensional (2D) electron structure. For example, at 1.54 eV$<E<$1.6 eV the DOS is almost constant as a function of energy (characteristic to 2D DOS) and around 1.52 eV$<E<$1.54 eV the DOS seems to be proportional to $1/\sqrt{E}$ (characteristic to 1D).

We calculated also the transverse ($y$ direction) part of the confinement energy as a function of $x$ coordinate. Figure 10 shows the relative transverse confinement enrgies in the CC [10(a)], CP1 [10(b)], and CP2 [10(c)] structures. The solid and dashed lines correspond to the electron and hole energies. The QWRS geometry is shown in the background as shaded areas. The transverse energies shows the effective potential energy of a charge carrier as a function of $x$ coordinate, since they contain the geometry, strain, and piezoelectric field.

## VIII. CONCLUSIONS

The electronic structure of a quantum wire superlattice in a corrugated (111) quantum well was studied using the eight-band $\mathbf{k}\cdot\mathbf{p}$ method. Atomic-level structure calculations show in accordance with the continuum model that the confinement effect is a complex interplay of the band edge discontinuity, strain, and piezoelectricity. The electromechanical coupling, studied within the elastic continuum model was found small. Confinement energies (with respect to the barrier band edge) up to 0.164 eV for electrons and 0.126 eV for holes were achieved by optimizing the structure.

There is little effect of the phase shift, between the two interfaces of the compressed CC structure, on the electronic properties. The electron (hole) wavefunction is only affected by the B (A) face of the corrugated QW, because in a compressed III-V the electric field is typically directed from the B (anion) face to the A (cation) face of the QW.[36] The wave functions do not extend over the whole 8 nm wide QW due to the piezoelectric field and therefore they do not sense the phase shift. The effect of the phase shift increases with decreasing $T_{QW}$ and with decreasing piezoelectric field. For the reported CC structure the phase shift can only separate elec-

trons and holes laterally (in $x$ direction) and it does not change the QWR confinement. From the results calculated for the strained CC and CP1 geometries we conclude that it is necessary to have a corrugated B (A) face in order to obtain a QWR-like localization of electrons (holes) if $T_{QW} \geqslant 8$ nm. If both electrons and holes are to be localized into QWRs either both interfaces should be corrugated or the thickness $T_{QW}$ should be less than 8 nm.

We studied the transverse ($y$ direction) part of the confinement energies as a function of $x$, for the three reported geometries. From this we conclude that the strain-induced effective QWR confinement potential, at a planar interface, is about 7 mV (5 mV) for electrons (holes), when $T_{QW}=8$ nm. The corrugation-induced QWR confinement potential for electrons (holes) is about 40 mV (27 mV) in a strained CP geometry. The strongest QWR confinement for electrons (holes) was obtained in the CP1 (CC) geometry. We conclude that the most important geometrical parameters to be tuned are the height of a corrugation step and the length of one corrugation period. These are both related to the offset angle $\theta$. The higher steps and the longer period, the smaller will the interwire coupling be.

We have shown that using the appropriate material parameters the spurious solutions of the electron structure calculations can be eliminated, without loosing the agreement with the bulk electronic dispersion. The observed spin splitting in asymmetric semiconductor heterostructures was explained by the lack of the inversion symmetry. To give a complete picture of the spin-splitting phenomenon in asymmetric semiconductor heterostructures further studies are required.

The calculated density of states of the CC structure showed that the QWRS is neither a two-dimensional QW nor a one-dimensional QWR structure, rather something in between. The density of electron states contained both flat regions where it was constant as a function of energy (characteristic to 2D DOS) and regions where it was proportional to $1/\sqrt{E}$ (characteristic to 1D). The density of valence states contained many sharp peaks, indicating that the density of states is very close to that of a QWR geometry. However, the absorption coefficient, showed only a small dependence on the polarization, indicating poor optical QWR properties, which is explained by the strong charge separation in the structure. The piezoelectric field makes it very difficult to study the absorption coefficient of the CC structure.

*Electronic address: fredrik.boxberg@tkk.fi

†Electronic address: teresh@lce.hut.fi

[1] H. Sakaki, Jpn. J. Appl. Phys. **19**, 735 (1980).

[2] H. Saito, K. Nishi, S. Sugou, and Y. Sugimoto, Appl. Phys. Lett. **71**, 590 (1997).

[3] M. S. Miller, H. Weman, C. E. Pryor, M. Krishnamurthy, P. M. Petroff, H. Kroemer, and J. L. Merz, Phys. Rev. Lett. **68**, 3464 (1992).

[4] F. Liu, J. Tersoff, and M. G. Lagally, Phys. Rev. Lett. **80**, 1268 (1998).

[5] L. Bai, J. Tersoff, and F. Liu, Phys. Rev. Lett. **92**, 225503 (2004).

[6] Y. Nakamura, S. Koshiba, and H. Sakaki, Appl. Phys. Lett. **69**, 4093 (1996).

[7] T. Melin and F. Laruelle, Phys. Rev. B **65**, 195302 (2002).

[8] A simple model of corrugated structure has been reported by T. Ishigaki, M. Ogawa, M. Morita, and T. Miyoshi, J. Appl. Phys. **91**, 5815 (2002). Their calculation neglects the piezoelectric effect, and is limited to four-band Luttinger–Kohn model.

[9] G. A. Baraff and D. Gershoni, Phys. Rev. B **43**, 4011 (1991).

[10] O. Stier and D. Bimberg, Phys. Rev. B **55**, 7726 (1997).

[11] Ansys 5.7.1, Inc., Swanson Analysis Systems, Houston, PA, 1998.

[12] P. N. Keating, Phys. Rev. **145**, 637 (1966).

[13] R. Martin, Phys. Rev. B **1**, 4005 (1970).

[14] J. Singh, *Physics of Semiconductors and Their Heterostructures* (McGraw-Hill, New York, 1993).

[15] K. Nordlund, P. Partyka, R. S. Averback, I. K. Robinson, and P. Ehrhart, J. Appl. Phys. **88**, 2278 (2000).

[16] C. Pryor, Phys. Rev. B **57**, 7190 (1998).

[17] O. Stier, *Electronic and Optical Properties of Quantum Dots and Wires* (Wissenschaft und Technik Verlag, Berlin, 2001).

[18] H. Jiang and J. Singh, IEEE J. Quantum Electron. **34**, 1188 (1998).

[19] M. G. Burt, J. Phys.: Condens. Matter **4**, 6651 (1992).

[20] D. Gershoni, C. H. Henry, and G. A. Baraff, IEEE J. Quantum Electron. **29**, 2433 (1993).

[21] ARPACK Users' Guide: Solution of Large-Scale Eigenvalue Problems with Implicitly Restarted Arnoldi Methods, Society for Industrial & Applied Mathematics, 1998.

[22] N. W. Ashcroft and N. D. Mermin, *Solid State Physics* (Sanders College, Hong Kong, 1987), p. 143.

[23] F. Boxberg, R. Tereshonkov, and J. Tulkki (unpublished).

[24] M. G. Burt, Superlattices Microstruct. **23**, 531 (1998).

[25] W. Jaskolski, R. Oszwaldowski, and G. W. Bryant, Vacuum **63**, 191 (2001).

[26] M. J. Godfrey and A. M. Malik, Phys. Rev. B **53**, 16504 (1996).

[27] C. S. Xavier, *Theoretical Methods for Spintronics in Semiconductors with Applications* (California Institute of Technology, Pasadena, CA, 2003).

[28] B. A. Foreman, Phys. Rev. B **56**, R12748 (1997).

[29] W. Trzeciakowski, Phys. Rev. B **38**, 12493 (1988).

[30] *Numerical Data and Functional Relationships in Science and Technology*, Landolt-Börnstein, New Series, Group III, Vol. 17a (Springer, New York, 1991).

[31] I. Vurgaftman, J. R. Meyer, and L. R. Ram-Mohan, J. Appl. Phys. **89**, 5815 (2001).

[32] L.-W. Wang, A. Zunger, and K. A. Mäder, Phys. Rev. B **53**, 2010 (1996).

[33] C. Pryor, J. Kim, L. W. Wang, A. J. Williamson, and A. Zunger, J. Appl. Phys. **83**, 2548 (1998).

[34] Y. A. Bychkov and E. I. Rashba, J. Phys. C **17**, 6039 (1984).

[35] G. Bastard, *Wave Mechanics Applied to Semiconductor Heterostructures* (Les Editions de Physique, Les Ulis, 1988).

[36] C. Mailhiot and D. L. Smith, Phys. Rev. B **35**, 1242 (1987).